

Pore formation during dehydration of a polycrystalline gypsum sample observed and quantified in a time-series synchrotron X-ray micro-tomography experiment

F. Fusseis^{1*}, C. Schrank², J. Liu^{3,4}, A. Karrech^{4,5}, S. Llana-Fúnez⁶, X. Xiao⁷, K. Regenauer-Lieb^{3,4,8}

¹ Institut für Geologie, Mineralogie und Geophysik, Ruhr-Universität Bochum, Germany

² School of Earth, Environmental and Biological Sciences, Queensland University of Technology, Brisbane, Australia

³ Western Australian Geothermal Centre of Excellence, Perth, Australia

⁴ CSIRO Earth Science and Resource Engineering, Kensington, Australia

⁵ School of Mechanical Engineering, University of Western Australia, Crawley, Australia

⁶ Departamento de Geología, Universidad de Oviedo, Oviedo, Spain

⁷ Advanced Photon Source, Argonne, USA

⁸ School of Earth and Environment, University of Western Australia, Crawley, Australia

* corresponding author: florian@fusseis.at

Abstract

We conducted an in-situ X-ray micro-computed tomography heating experiment at the Advanced Photon Source (USA) to dehydrate an unconfined 2.3 mm diameter cylinder of Volterra Gypsum. We used a purpose-built X-ray transparent furnace to heat the sample to 388 K for a total of 310 minutes to acquire a three-dimensional time-series tomography dataset comprising nine time steps. The voxel size of 2.2 μm^3 proved sufficient to pinpoint reaction initiation and the organization of drainage architecture in space and time. We observed that dehydration commences across a narrow front, which propagates from the margins to the centre of the sample in more than four hours. The advance of this front can be fitted with a square-root function, implying that the initiation of the reaction in the sample can be described as a diffusion process. Novel parallelized computer codes allow quantifying the geometry of the porosity and the drainage architecture from the very large tomographic datasets (2048³ voxels) in unprecedented detail. We determined position, volume, shape and orientation of each resolvable pore and tracked these properties over the duration of the experiment. We found that the pore-size distribution follows a power law. Pores tend to be anisotropic but rarely crack-shaped and have a

Florian Fusseis 1/17/12 12:36 PM

Deleted: radiation based

Florian Fusseis 1/17/12 12:36 PM

Deleted: -3*+,

Florian Fusseis 1/17/12 12:36 PM

Deleted: Schrank¹⁻³

Florian Fusseis 1/17/12 12:36 PM

Deleted: Liu^{1,2}, A. Karrech¹

Florian Fusseis 1/17/12 12:36 PM

Deleted: Fúnez⁵

Florian Fusseis 1/17/12 12:36 PM

Deleted: Xiao⁶

Florian Fusseis 1/17/12 12:36 PM

Deleted: Lieb¹⁻

Florian Fusseis 1/17/12 12:36 PM

Formatted: Superscript

Florian Fusseis 1/17/12 12:36 PM

Deleted: ¹ Multi-scale Earth System Dynamics, Perth, Australia

Florian Fusseis 1/17/12 12:36 PM

Deleted: Environment,

Florian Fusseis 1/17/12 12:36 PM

Deleted: Western Australia, 35 Stirling Highway, Crawley WA 6008

Florian Fusseis 1/17/12 12:36 PM

Deleted: ⁵

Florian Fusseis 1/17/12 12:36 PM

Deleted: ⁶

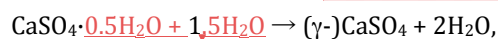
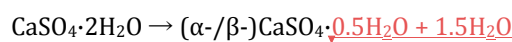
Florian Fusseis 1/17/12 12:36 PM

Deleted: ⁺ now at Institut für Geologie, Mineralogie und Geophysik, Ruhr-Universität Bochum, Germany

preferred orientation, likely controlled by a pre-existing fabric in the sample. With on-going dehydration, pores coalesce into a single interconnected pore cluster that is connected to the surface of the sample cylinder and provides an effective drainage pathway. Our observations can be summarized in a model in which gypsum is stabilized by thermal expansion stresses and locally increased pore fluid pressures until the dehydration front approaches to within about 100 μm . Then, the internal stresses are released and dehydration happens efficiently, resulting in new pore space. Pressure release, the production of pores and the advance of the front are coupled in a feedback loop.

1. Introduction

Since Heard and Rubey (1966) associated the dehydration of gypsum with a significant strength drop of the material, the reaction is often considered a model for the processes related to prograde devolatilization in tectonics and metamorphic geology. A wealth of studies was conducted to understand the mineralogy of the apparently simple reaction, but despite great efforts over the last hundred years or so, Charola et al. (2007), in their review of gypsum deterioration, had to point out that “a comprehensive approach to understand the true nature and behaviour of this ubiquitous compound [...] is still missing”. There seems to be consensus that the dehydration of gypsum is a two-step process:



in which gypsum, upon heating to temperatures larger than $\sim 373\text{ K}$ first dehydrates into the metastable hemi-hydrate, which then dehydrates into γ -anhydrite (Bezou et al., 1995, Singh and Middendorf, 2007, Christensen et al., 2008, Jacques et al., 2009). The existence of a subhydrate $\text{CaSO}_4 \cdot x\text{H}_2\text{O}$ has been discussed for some time, and recently Schmidt et al., (2011) proved that hemihydrate reacts to $\text{CaSO}_4 \cdot 0.625\text{H}_2\text{O}$ in moist conditions. The dehydration of gypsum is an anomalously slow process compared to the dehydration of other compounds containing crystal water (Charola et al., 2007).

This paper focuses on the initiation of dehydration at 388 K. At the temperature and time scales of our experiment, hemihydrate is expected to be the most common dehydration product (Freyer and Voigt, 2009). Two hemi-hydrate varieties are distinguished on the basis of their specific surface area, crystal sizes, habit and surface topography of the crystals (Freyer and Voigt, 2003, 2009, Singh and Middendorf, 2007). Where the dehydration reaction occurs under a

Florian Füsseis 1/17/12 12:36 PM

Deleted: We discuss our findings in the context of previous studies.

Florian Füsseis 1/17/12 12:36 PM

Deleted: $1/2\text{H}_2\text{O} + 3/2\text{H}_2\text{O}$

Florian Füsseis 1/17/12 12:36 PM

Deleted: $2\text{H}_2\text{O} + 3/2\text{H}_2\text{O}$

Florian Füsseis 1/17/12 12:36 PM

Deleted: 100°C

Florian Füsseis 1/17/12 12:36 PM

Deleted: first part

Florian Füsseis 1/17/12 12:36 PM

Deleted: reaction,

Florian Füsseis 1/17/12 12:36 PM

Deleted: formation of hemi-hydrate from gypsum.

105 high partial water vapor pressure in acidic solutions, α -hemi-hydrate forms. β -
106 hemi-hydrate results from dehydration under dry conditions or in vacuum. By
107 comparison, Hildyard et al. (2011) identified euhedral hemi-hydrate crystals in
108 polycrystalline gypsum samples that were dehydrated at low confining and
109 effective pressures as α -hemi-hydrate (their experiments GYP37 and 38). The
110 hemi-hydrate grains formed inequigranular, decussate aggregates.

111
112 Several models have been proposed as to how the reaction would progress in a
113 polycrystalline sample (Olgaard et al., 1995, Ko et al., 1997, Miller et al., 2003,
114 Wang and Wong, 2003). The model of Olgaard et al. (1995), refined in Ko et al.
115 (1997), is probably based on the largest experimental dataset. Interpreting syn-
116 experimental fluid expulsion measurements and micrographs made post-
117 experimentally, they predicted dehydration to advance in three stages: a first
118 stage, where the reaction commences throughout the sample but the released
119 fluid is trapped in isolated pores, thus leading to high pore fluid pressures. In a
120 second stage these pores are thought to interconnect and form a permeable
121 network while fluid expulsion increases strongly. In a third stage, fluid expulsion
122 decreases and the reaction comes to completion. Wang and Wong (2003)
123 | investigate this model numerically. They predict that dehydration occurs at a
124 reaction front that propagates across a 25mm long sample in less than 200
125 minutes. Porosity increases smoothly across the entire length of the sample.
126 Even though Wang and Wong duplicate the fluid-expulsion curves of Ko et al.
127 (1997) quite accurately, their results contrast with earlier descriptions of very
128 sharp reaction fronts in dehydrating gypsum specimens by Stretton (1996). In
129 her Plate 11.1, Stretton shows a partly reacted sample where the dehydration
130 | initiates across a narrow zone less than 50 μ m wide.

131
132 Because the fluid volume (V_{fluid}) increases slightly more than the solid volume
133 | (V_{solid}) decreases during the reaction ($|\Delta V_{\text{fluid}}/\Delta V_{\text{solid}}|=1.\underline{23}$), pore fluid pressure
134 is considered critical for the reaction progress, the formation of drainage
135 pathways and fluid escape (e.g., Heard and Rubey, 1966, Murrell and Ismail, 1976,
136 Ko et al., 1997, Llana-Fúnez et al., submitted). Miller et al. (2003) propose a
137 model where hydraulic fracturing resulting from fluid overpressure exclusively
138 controls drainage. Applying Hacker's (1997) classification, the dehydration
139 reaction is fluid-dominated and driven by a decreasing pore fluid pressure.
140 Llana-Fúnez et al. (submitted) associate fluid expulsion with reaction progress
141 and show that a decreasing pore fluid pressure accelerates the reaction. It is
142 known that the reaction is strongly pressure sensitive (McConnel et al., 1987,
143 Karrech et al., in prep.) and only proceeds where pore fluid pressures are

Florian Füsseis 1/17/12 12:36 PM

Deleted: across

Florian Füsseis 1/17/12 12:36 PM

Deleted: micron

Florian Füsseis 1/17/12 12:36 PM

Deleted: 3

relieved by water draining from the reaction site (Miller et al., 2003, Llana-Fúnez et al., submitted). This renders the formation of permeable porosity critical for the reaction progress (Olgaard et al., 1995) and a hinge for all models of dehydration of polycrystalline gypsum.

All current models for dehydration of polycrystalline gypsum under drained conditions are based on the indirect assessment of reaction progress and porosity formation through fluid expulsion and the post-experimental, two-dimensional analysis of reaction fabrics in samples reacted to different extents. These are obvious limitations that were acknowledged by previous authors (Ko et al., 1997, Wang and Wong, 2003).

Here we apply a novel workflow that allows documenting the reaction progress in situ in three dimensions with high temporal and spatial resolution. We conducted a drained heating experiment in an X-ray transparent furnace and monitored reaction progress with synchrotron radiation based X-ray micro-computed tomography to acquire a volumetric time-series data set of the porosity evolution during dehydration. By documenting all pores larger than $2.2\mu\text{m}^3$ in volume, the tomographic time series data allow to precisely document the reaction. We quantify the progress of the dehydration front and analyse the organization of the drainage architecture in space and time.

2. Materials and methods

2.1 Volterra Gypsum

We cored a 2.3 by 8 mm cylinder from a block of Alabaster from Volterra, Italy. This polycrystalline material has become a standard for gypsum dehydration experiments (e.g., Ko et al., 1995, [Olgaard et al., 1995](#), Miller et al., 2003, Llana-Fúnez et al., submitted). Stretton (1996) determined a mean grain size of $120\mu\text{m}$ using a line intercept method on thin sections.

We used the intercept software of Launeau et al. (2010) to determine mean grain size and to analyse shape anisotropy in both secondary electron images taken from polished sections and photographs of thin sections acquired under polarized light and with crossed polarisers. The mean grain size of Volterra gypsum is between 45 and $123\mu\text{m}$ (Table 2). Using this grain size interval, we estimate that the imaged part of our sample contains between 10,000 and 60,000 grains. Thin sections reveal that the material can be fairly heterogeneous locally (Suppl. Figure 1). The aspect ratios of shape-fabric ellipsoids range from 1.09 to 1.52, indicating local shape-preferred orientations. Pockets of platy high-

Florian Füsseis 1/17/12 12:36 PM

Deleted: Our data support a model where internally created pressures stabilize gypsum. The reaction only proceeds where these pressures can be relieved. This happens efficiently over a narrow dehydration front whose slow advancement can be described by a linear partial differential diffusion equation. A large interconnected pore cluster dominates the drainage architecture and links the exterior of our unconfined sample to the dehydration front at all times. Our observations suggest that under unconfined, drained conditions, hydraulic fracturing does not control the sample drainage. We conclude with an attempt to reconcile our observations with current models. ... [1]

Florian Füsseis 1/17/12 12:36 PM

Deleted: Oolgaard

Florian Füsseis 1/17/12 12:36 PM

Deleted: micron,

Florian Füsseis 1/17/12 12:36 PM

Formatted: Font color: Black

Florian Füsseis 1/17/12 12:36 PM

Deleted:

aspect ratio gypsum crystals were found to cover areas of a few square millimetres in size (Suppl. Figure 1). We have no indication that our tomographic sample is composed of grains of this size.

2.2 Synchrotron Tomography

We used synchrotron radiation based X-ray micro-computed tomography (SR μ CT) to document the progress of gypsum dehydration in 3 dimensions. SR μ CT is based on two-dimensional digital radiographs that record the attenuation of coherent X-rays penetrating a sample. The attenuation of X-rays is a material property related to density; hence in compositionally heterogeneous samples the recorded X-ray absorption varies spatially. Radiographs shot from changing viewpoints are combined, using reconstruction algorithms, in a three-dimensional model of the distribution of different materials in a specimen (e.g. Stock, 2009), in our case gypsum, hemi-hydrate and pores. During reconstruction, the spectrum of absorption values recorded in a sample is mapped into a 32-bit gray value space (2^{32} gray levels mapped into the numeric interval from -0.008 to 0.008). Several tomographic datasets acquired at different points in time from the same dehydrating polycrystalline gypsum sample can be merged in a four-dimensional (i.e. a time series) dataset.

Microtomographic data were collected at the bending magnet beam line 2-BM at the Advanced Photon Source, Argonne National Laboratory, USA. A double multilayer monochromator of 1.5 % bandwidth provided 27 KeV X-rays; images were collected in transmission mode by a CCD camera behind the sample in the hutch configuration. Data were collected through rotating the samples in steps of 0.125° over 180°. The acquisition time for each data set was about 25 minutes, which allowed for nine scans during the experimental run.

2.3 In-situ heating experiment

For the experiment, we used an X-ray transparent furnace that was installed within the tomographic setup (Figure 1). The furnace consists of a hollow cylinder, made from Al₂O₃ ceramic, 10*30 mm in dimension, with a lid to limit the heat loss. The wall thickness of the cylinder is 1.5 mm. X-rays are allowed to penetrate the sample through two uncovered rectangular windows (4x4 mm) 3 mm from the bottom edge of the furnace. Two heating wires, coiled around the cylinder above and below the windows, heat the furnace. The sample, which was glued to a 25x25x13 mm Al-Si ceramic block at its base, was inserted into the furnace from the bottom. The ceramic base block insulated the rotation stage from the heat above. We rotated the entire lower assembly, which included the

stage, the base block and the sample, for data acquisition. A thermocouple was mounted to the base of the sample cylinder. For all glued connections (heating coil and sample mounting, thermocouple installation) we used high-temperature Sauereisen No. 7 cement.

We heated the sample to 388 K for a total of 310 minutes (Suppl. Figure 2). The experiment began with short heating periods (1, 2, 3 and 4 minutes), followed by five heating periods of 60 minutes each. In between each heating period, the reaction had to be suspended for data acquisition, and the sample was passively cooled to 323 K in about 2-3 minutes (Suppl. Figure 2). After each scan, the furnace was heated to reaction temperatures in 46 s (ramp rate 150° min⁻¹). The experiment yielded a total of nine datasets (i.e. time steps). Before and after data acquisition, the sample experiences temperature fluctuations of 65 K that propagate through the cylinder. The time it takes for the sample to equilibrate thermally after each scan can be calculated from the thermal diffusivity and the dimension of the sample (Clauser and Huenges, 1995, Regenauer-Lieb and Yuen, 2004): $t = 4r^2/D_T$, where t is the time scale, r is the sample radius and D_T is the thermal diffusivity. For a thermal diffusivity of gypsum of $0.285 \times 10^{-6} \text{ m}^2 \text{ s}^{-1}$ (Clauser and Huenges, 1995) and a sample radius of 1.3 mm this indicates thermal equilibration in less than 20 seconds. This allows us to conclude that diffusion of heat (i.e., a thermal gradient) does not influence the kinetics of the reaction in our sample. All times given in the further text are *minutes at 388 K*, the reaction temperature.

A dummy sample was employed to train a *Eurotherm 2404* controller to heat the specimen with a precision of about 1°. Only one thermocouple was used in the experiment, and we have no information on the temperature distribution in the furnace. While air was certainly circulating through the openings in the furnace we believe that the very responsive heater and the small dimension of the sample prevented major temperature gradients across the sample.

Gypsum dehydration has been studied in numerous experiments under a large range of boundary conditions and excellent reproducibility of experiments was demonstrated. Given the significant costs and efforts that it took to conduct the experiment reported here, we restrict ourselves to a single sample specimen. We are confident that our principal findings can be reproduced.

2.4 Data processing and analysis

Three-dimensional models were reconstructed from 1440 tomographic

Florian Füsseis 1/17/12 12:36 PM

Deleted: degrees

Florian Füsseis 1/17/12 12:36 PM

Deleted: using

Florian Füsseis 1/17/12 12:36 PM

Deleted: diffusion length scale

Florian Füsseis 1/17/12 12:36 PM

Formatted: Font color: Black

Florian Füsseis 1/17/12 12:36 PM

Deleted: We did, however, observe that the reaction progressed asymmetrically in the sample (see below). This possibly reflects some heat loss through the thermocouple and the cement that was used to hold it in place (see discussion).

295 projections/time step for all nine time steps of this study using Advanced Photon
296 Source in-house algorithms and facilities. Each projection image comprises
297 2048x1536 pixels in raw format and each reconstructed three-dimensional
298 dataset is discretized into a stack of 1536 horizontal image slices with a vertical
299 spacing of 1.3 μm . During 3D rendering, these image slices are combined in a
300 volumetric dataset consisting of 2048x2048x1536 voxel. The minimum effective
301 pixel size achieved was 1.3 μm , yielding a volume of 2.2 μm^3 per voxel. All of our
302 datasets proved of excellent quality, with a minimum of noise and artefacts. The
303 data document a 2 mm section out of the upper half of the specimen cylinder,
304 just above the thermocouple; the top of the cylinder is not included in the
305 dataset.

306

307 The X-ray absorption of gypsum and hemi-hydrate proved sufficiently different
308 from water and air to clearly distinguish pores from minerals, and the achieved
309 spatial resolution is sufficient to do so (Figure 2). It is difficult to distinguish
310 Gypsum and hemi-hydrate in the reacted part of the sample.

311

312 We use the term *pore* for any void space irrespective of the shape and size (cf.
313 Sprunt and Brace, 1974). Due to their low X-ray attenuation, pores occupy the
314 low end of the grey value histogram derived from a tomographic dataset (Figure
315 3). We segmented pores from solids by binary thresholding. The process, which
316 requires the determination of a critical threshold, separates all voxels into those
317 that belong to pores and those that do not.

318

319 For binary thresholding, determining the correct threshold value is critical
320 (Kaestner et al., 2008 and references therein). In our case the reaction affects the
321 grey value distribution and we found that we could use these changes to
322 accurately determine the threshold value (Figure 3). For all time steps, we
323 calculated histograms of the grey value frequency distribution from 180 million
324 voxels that constitute a parallelepiped just off the centre of the sample cylinder
325 (400x600x750 voxel³ or 520x780x975 μm^3). As the reaction proceeded through
326 the parallelepiped, hemihydrate and pores formed, and consequently voxels
327 were reassigned amongst the 1024 bins constituting the histogram. Hemihydrate

328 is denser than gypsum; therefore voxels that were gypsum and become
329 hemihydrate assume a grey-value greater than that of gypsum. In the histogram,
330 these voxels will increase the 'height' of the bright right shoulder (Figure 3). On
331 the other hand, pores, water- or gas-filled have a much lower density than
332 gypsum and hemihydrate. Therefore, voxels that were gypsum and turned into
333 pores will attain grey values smaller/darker than that of gypsum and

Florian Füsseis 1/17/12 12:36 PM

Deleted: microns

Florian Füsseis 1/17/12 12:36 PM

Deleted: slightly

Florian Füsseis 1/17/12 12:36 PM

Deleted: values equal or

Florian Füsseis 1/17/12 12:36 PM

Deleted: they

hemihydrate. They will increase the frequency of dark voxels and hence contribute to the dark left shoulder of the histogram (Figure 3). This low-absorption shoulder is delimited by an intersection point of all histograms at a grey value of 0.00018 (inset in Figure 3), which separates the brighter bins occupied by gypsum voxels from darker bins of pore voxels. We used this value to segment pores from gypsum and hemihydrate in all datasets.

All pores in the above-mentioned parallelepiped were analysed. We use the method of Liu et al. (2009) to label face-connected clusters of 'porous' voxels as individual pores. We calculate the position, volume, surface, shape and orientation of each individual pore. In the datasets obtained after prior to heating and 10, 70, 130, 190, 250 and 310 minutes at reaction temperature, we determined frequency distributions for pore size, pore shapes, pore orientation and performed a percolation analysis.

We furthermore used a moving window method to analyse the porosity increase along a radius of the sample in the dataset obtained after 10, 70 and 130 minutes. We migrated a 20x400x750 voxel large box along the x-axis across the dehydration front described below. The radius was chosen so that the front was crossed in sections with low curvature. We used a step size of 1 voxel, and quantified the porosity in each box. We ascribe the fact that, in this analysis, we recorded porosity values that exceed the theoretically expected 29 % to result from the narrow sampling box combined with a locally heterogeneous distribution of porosity.

Two error sources affect SR μ CT data: errors introduced during data acquisition and reconstruction (Banhart, 2008) and the common discretization error of raster data (e.g. Arns et al., 2002). We estimated the combined error conservatively by assuming that the surface of each pore is subject to an uncertainty of \pm one voxel with respect to the surface normal vector. Since the topology of pore space is very complex, we determined this error empirically by a numerical dilation/erosion experiment: we expanded and shrank each pore in the parallelepiped by one voxel on their outer faces (Liu & Regenauer-Lieb, 2011) and then quantified the respective changes in the data. Apart from returning error margins for our quantification, this test provides insight into the pore structure and we discuss the results below. We stress that these error margins significantly overestimate the true error.

The data were visualized using the imaging software Avizo Fire.

377

378 3. Results

379 The following chapter is subdivided into two parts: A first part (Subsection 3.1)
380 describes the two textural domains we identified in the data and the dehydration
381 front that separates them. We quantified the advance of this front in the sample
382 over time to assess the reaction progress through dehydration initiation. In a
383 second part (Subsection 3.2) we analyse the porosity evolution behind the
384 dehydration front to characterize the drainage architecture in the sample and its
385 evolution during the experiment.

386

387 3.1 Dehydration initiation

388 | The tomographic data acquired of the partly dehydrated ~~sample~~ reveal two
389 textural domains, separated by a narrow boundary (Figure 2). The inner textural
390 domain shows a relatively homogeneous X-ray absorption. Based on the
391 histogram obtained from the unreacted sample (Figure 3) the attenuation
392 pattern in the inner domain is attributable to gypsum. The outer textural domain
393 shows a more heterogeneous and wider absorption distribution resulting from
394 abundant porosity in between the (denser) solid phases, gypsum and hemi-
395 hydrate (Figures 2). Over the course of our experiment the relative widths of
396 these domains change and the narrow boundary separating them migrates
397 steadily inwards from the periphery of the sample cylinder (Figure 2).

398

399 We use the porosity, which is indisputably a result of the reaction, as a proxy for
400 the onset of dehydration. As only very few pores were documented in the inner
401 domain (Figure 2), we infer that, on the scale that we could resolve in the
402 tomographic datasets, gypsum is stable there. Consequently we interpret the
403 advancing boundary between the inner and the outer textural domain as a
404 dehydration front that delimits the gypsum stability field spatially. The front
405 marks the point where, on the scale of observation, gypsum becomes unstable
406 and dehydration advances rapidly. The dehydration front itself exhibits a steep
407 porosity gradient (Figure 4). Porosity increases from between 2.7 and 6.8 % to
408 about 30 % over a distance of 100 - 200 μm . The gradient remains similar over
409 the duration of the experiment.

410

411 We tracked the progress of the dehydration front in two horizontal and two
412 vertical tomography slices at times ~~3, 6, 10, 70, 130~~ and ~~190 minutes~~ (Figures
413 ~~5a,b~~). We measured the cumulative radial propagation, $r_\alpha(t)$, of the dehydration
414 front. $r_\alpha(t)$ denotes the distance that the dehydration front has travelled over the
415 time t from the sample margin along a radial line of orientation α (Suppl. Figure

Florian Füsseis 1/17/12 12:36 PM

Deleted: samples

Florian Füsseis 1/17/12 12:36 PM

Deleted: 3', 6', 10', 70', 130'

Florian Füsseis 1/17/12 12:36 PM

Deleted: 190'.

3). The long axis of the cylindrical sample is defined as Z-axis. Radii are defined as lines in the plane normal to Z that connect the sample margin and the centroid of the unreacted domain. In horizontal slices, we determined $r_{\alpha}(t)$ in steps of 0.5° for the interval $[0^{\circ}; 360^{\circ}]$ at a given height z_i . We chose horizontal slices located in the middle of the sample volume (at $\sim Z/2$) to avoid early interference with the dehydration front propagating inward from the top surface of the sample. The vertical slices represent the XZ- and the YZ-plane of the sample, respectively, and cover the entire height of the imaged sample volume. Hence, the orientations of the considered radii are 0° and 180° for the XZ-plane and 90° and 270° for the YZ-plane (Suppl. Figure 3). In each vertical slice, radial progress was determined not only for two opposite orientations but also at different vertical positions. We used a vertical step size Δz of $13 \mu\text{m}$ for each pair of measurements (Suppl. Figure 3). In addition, the temporal evolution of the proportion of dehydrating area with respect to total sample area was calculated for the horizontal slices (Suppl. Figure 4).

The results show that the dehydration front propagates in a non-linear fashion (Figure 5). It moves faster in the beginning of the experiment and slows down subsequently. There is a marked asymmetry in dehydration front progress. The front moves faster in the right side of the sample in the XY-plane (i.e., the clockwise orientation interval $[270^{\circ}; 90^{\circ}]$, Figure 5a). In other words, the centroid of the unreacted domain does not coincide with the centroid of the sample cylinder. We used a non-linear least squares method to fit the results with a linear diffusion function of the type

$$\bar{r}_{\alpha}(t) = \sqrt{Dt}, \quad [1]$$

where $\bar{r}_{\alpha}(t)$ is mean distance of front to sample margin, D is a constant diffusivity, and t is time. We obtain a D of $8.29 \times 10^{-11} \text{ m}^2\text{s}^{-1}$ with $r^2 = 0.71$ if we fit Eq. 1 to all data (Figure 5c).

The initially smooth front exhibits a variable roughness with a trend to irregularities with higher amplitudes later during the experiment (Figures 2 and 5a). The wavelength of these front indentations, 20 to $100 \mu\text{m}$, is of the same order of magnitude as the mean grain size of the sample (cf. Table 1). None of the undulations persists beyond one hour. In cases, individual cusps become narrow plumes of μm -sized pores extending up to $200 \mu\text{m}$ into unreacted gypsum. In three dimensions, these 'plumes' are irregular porous sheets that are usually directly connected to a large pore in the outer domain. In the very early stages of the experiment, we did observe an alignment of these plumes with some of the cracks described below. The plumes occasionally surround volumes that are left

Florian Füsseis 1/17/12 12:36 PM

Deleted: micron

Florian Füsseis 1/17/12 12:36 PM

Deleted: $x(t)$

Florian Füsseis 1/17/12 12:36 PM

Deleted: $x(t)$

Florian Füsseis 1/17/12 12:36 PM

Deleted: micron

462 behind by the moving dehydration front. In these volumes, porosity increases
463 with time.

464

465 Over the first three hours we found isolated crack-like features in the specimen.
466 The width of these features is at the resolution limit, their longitudinal extent up
467 to several hundred um. They showed no preferred orientation. We did not see an
468 increase in their number, or width, as the experiment progressed. Neither did we
469 see any porosity associated with the features apart from a few very early pores
470 following them at the periphery of the sample. Based on Stretton's (1996) and
471 Milsch and Scholz's (2005) reports on the deformation microstructures
472 developed in gypsum we are uncertain whether these features are cracks. As
473 they did not affect the reaction progress we do not consider them any further.

474

475 | 3.2 The porosity and drainage architecture during dehydration

476 | 3.2.1 Porosity

477 | Visual inspection of the porosity in the dehydrating domain indicates that the
478 porosity consolidates rapidly once the front has passed (Suppl. Figure 4). We
479 quantified the temporal evolution of porosity in the parallelepiped to better
480 understand this consolidation and the geometry of the dehydration architecture.
481 The porosity evolution is summarized in Table 2 and Figures 6 to 8.

482

483 The unreacted sample exhibits a porosity of 2.32 % (Figure 6a), which is
484 somewhat higher than the previously published figures for Volterra gypsum (0.5
485 %, Ko, 1993, 0.1 %, Stretton, 1996) and probably related to different
486 measurement techniques and minor local variations in porosity. As the reaction
487 front propagates through the parallelepiped, the total porosity increases. After
488 130 minutes, when the front has propagated through the parallelepiped, the
489 porosity peaks at 25.67 %. The porosity then decreases slightly to 24.01 % over
490 the next three hours. Both values are remarkably close to the theoretically
491 predicted 29% (e.g., Ko et al., 1997), which we consider an indication that the
492 critical threshold used for segmentation of the data is appropriate.

493

494 The total number of pores is very high in the unreacted dataset (> 2.1 million,
495 Figure 6b), increases at first as the dehydration front propagates into the sample
496 (10 minutes) but then decreases to 0.53 million after 130 minutes. Over the next
497 three hours it increases again to reach 0.63 million after 310 minutes, indicating
498 that more pores accommodate slightly less porosity. The observed changes in
499 total porosity and the number of pores once the front has passed (130 minutes)
500 are subtle and within the discretization error. The datasets from the numerical

Florian Füsseis 1/17/12 12:36 PM

Deleted: microns

Florian Füsseis 1/17/12 12:36 PM

Deleted: observation that gypsum is very unlikely to crack but will rather deform crystal-plastically, even at moderate temperatures,

Florian Füsseis 1/17/12 12:36 PM

Deleted: outer domain:

Florian Füsseis 1/17/12 12:36 PM

Deleted: outer

Florian Füsseis 1/17/12 12:36 PM

Deleted: .

Florian Füsseis 1/17/12 12:36 PM

Deleted: passed

expansion/shrinking experiment essentially mirror this evolution of the total porosity, despite the obviously quite different absolute values (Figure 6a). Expansion reduces the total number of pores at all times, while shrinking increases them to a level above the original data after 130 minutes (Figure 6b). This indicates that pores formed during the reaction are not isometric, so that shrinking leads to a break up into several smaller pores. Furthermore it shows that they are close enough to each other so that expansion by just one voxel joins neighbouring pores.

The pores in the outer domain span a wide range of sizes, from one to a maximum of 43 million voxel. Porosity in the unreacted sample is comprised of a large number of very small pores (Figure 7); pores smaller than $100 \mu\text{m}^3$ make up more than 95 % of the total porosity (Figure 8), with pores smaller than $5 \mu\text{m}^3$ contributing more than 50 % of the porosity. The pore size frequency distribution evolves from the unreacted one until it assumes a characteristic shape and position after 130 minutes (Figure 7). After that, the changes are subtle but marked by an increase of especially the smallest pores (inset in Figure 8). While after 130 minutes the contribution of pores smaller $1000 \mu\text{m}^3$ is only 6 % of the total porosity, the value increases to about 8 % after 310 minutes.

The dehydration-related porosity is characterized by the formation of one very large pore after 70 minutes (Figure 9). This topologically very complex pore accounts for more than 90 % of the total porosity (Table 2, Figure 8). It is four orders of magnitude larger than the second largest pore, intersects all faces of the parallelepiped and seems responsible for drainage of the volume. A visualization of this pore in a horizontal cross section shows that it connects the sample margin with the reaction front (Suppl. Figure 4).

As indicated by the shrinking test, the pores formed during dehydration are not isometric and this does not change over the course of the experiment. We characterize the shape of a pore by its isotropy index (i_i), which is defined as $i_i = e_3/e_1$, with e_1 and e_3 being the largest and smallest eigenvalue, respectively, of the orientation matrix of a pore as defined in Liu et al. (2009). $i_i = 1$ denotes an isotropic shape, while 'cracks' in the definition of Sprunt and Brace (1974) have i_i equal to or smaller than 0.1.

For this analysis we only consider pores larger than 50 voxel to minimise shape artefacts resulting from the limited possibilities to approximate the shape of small pores by a small number of (cubic) voxels. We also excluded pores larger

Florian Füsseis 1/17/12 12:36 PM

Deleted: minimize

Florian Füsseis 1/17/12 12:36 PM

Formatted: Font: Cambria

Florian Füsseis 1/17/12 12:36 PM

Formatted: Font: Cambria

Florian Füsseis 1/17/12 12:36 PM

Formatted: Font: Cambria

Florian Füsseis 1/17/12 12:36 PM

Deleted: due

Florian Füsseis 1/17/12 12:36 PM

Formatted: Font: Cambria

Florian Füsseis 1/17/12 12:36 PM

Deleted: the raster effect

552 than 1200 voxel, as their shapes are too complex to be accurately described by
553 the method (cf. [Suppl. Figure 5](#)). Our analysis shows that after 130 minutes 78 %
554 of the pores have an isotropy index smaller than 0.5 but larger than 0.2 (Figure
555 10). There is a tendency for larger pores to being more anisotropic. After 130
556 minutes only 0.6 % of all pores have isotropy indices equal to or smaller 0.1.
557 After 310 minutes, 0.4 % of pores have isotropy indices of 0.1 or smaller,
558 whereas 80.1 % have isotropy indices between 0.2 and 0.5.

559

560 3.2.2 Drainage architecture

561 The grain shape analysis we conducted on Volterra alabaster indicated a slight
562 shape-preferred orientation of grains (Table 1). To test the influence of such a
563 pre-existing fabric on the evolving porosity, we determined the orientations of
564 pores of three different size fractions (51-150 voxel, 151-300 [voxel](#) and 301-450
565 voxel) at different times during the experiment. The orientation of a pore is
566 represented by azimuth and dip angle of e_i with respect to the coordinate system
567 (Figure 2). Figure 11 illustrates the orientation of pores in the subsampled
568 parallelepiped prior to heating, after 70 minutes and after 310 minutes. The
569 orientations from the latter two datasets show the preferred alignment of pores
570 along a great circle at an angle of about 30 degrees to the xz-plane, with a
571 maximum close to the x-axis. Albeit weaker, due to the smaller of number of
572 pores, this trend can already be seen in the sample prior to heating (Figure 11a).
573 In the datasets acquired during dehydration, pores of all three size-fractions
574 follow this trend. The maximum density of e_i orientations of the smallest size
575 fraction (expressed through the contour lines in Figure 11b and c) rotates,
576 within the xy-plane, into the great circle between 70 and 310 minutes.

577

578 The cumulative pore size frequency distribution indicates that, soon after the
579 dehydration front has [passed, pores interconnect](#). We conducted a percolation
580 analysis to investigate this observation further. Percolation here refers to the
581 connectivity of pores (Stauffer and Aharony, 1994). A moving window method
582 was used (Liu et al., 2009), where cubes of various side lengths (25, 50, 100 and
583 200 voxel) are moved through the segmented datasets with a step size of 5 voxel.
584 For each cube position the porosity in the cube and pore connectivity in the
585 principal directions of the coordinate system are determined. For a given cube
586 size, the analysis yields the porosity frequency distribution for all cube positions
587 (Figure 12), as well as probability functions for percolation in the principal
588 directions for all cube placements (Figure 13).

589

590 The porosity frequency distribution illustrates how homogeneously porosity is

Florian Füsseis 1/17/12 12:36 PM

Deleted: 9

Florian Füsseis 1/17/12 12:36 PM

Formatted: Subscript

Florian Füsseis 1/17/12 12:36 PM

Formatted: Subscript

Florian Füsseis 1/17/12 12:36 PM

Deleted: a single pore drains the volume

Florian Füsseis 1/17/12 12:36 PM

Deleted: migrated through a volume

distributed in the sampling volume (Figure 12). The more heterogeneously porosity is distributed, the wider the porosity frequency distribution will be. Vertical lines mark the total porosities measured in the parallelepiped (Table 2) for reference. The distributions of porosities amongst the cube placements for the datasets from 130 to 310 minutes are narrow and have their maxima within 2.5 % of the measured total porosities. The frequency distributions derived from the 10 [min](#) and 70 [min](#) datasets reflect a comparatively large variability amongst the cubes, which is due to the circumstance that the dehydration front is still propagating through the parallelepiped at these times.

The spatiotemporal ability of a volume to drain is controlled by the degree of interconnectivity of pore space. Probability functions for percolation in the three principal directions for each time step describe the time-dependent evolution of percolation in the parallelepiped. Each of the four diagrams in Figure 13 compares the probabilities for percolation in a 50x50x50 voxel cube with a given porosity for two successive time steps. It becomes evident that the differences between the probability functions for the three directions are subtle, particularly after 130 minutes, and cubes with a porosity of 20% or more are percolating in all three directions with a probability of more than 90%. However, cubes with porosities below ~19 % are more likely to percolate in the x-direction.

4. Interpretation and discussion

In-situ SR μ CT time-series experiments and their quantitative analysis provide a novel way of studying tectono-metamorphic processes, fluid-rock interaction and secondary porosity. Despite its comparatively simplistic setup, our experiment overcomes the 'black box' limitations of previous experimental studies and maps a way towards the discrete characterization of metamorphic dehydration. Our results provide detailed insight into the advance of dehydration in polycrystalline gypsum, the porosity-forming mechanism and the influence of pre-existing fabric anisotropy on drainage [at atmospheric pressures](#).

4.1 Dehydration initiation

Confirming previous observations, our tomographic data show that the dehydration reaction propagates radially from the outer surface of the sample, where the water released during the reaction can escape, to the sample centre (Figure 2, e.g. Ko et al., 1997, Miller et al., 2003, Llana-Fúnez et al., 2007). A dehydration front delimits the drained portion of the sample (Figures 2, 4, 5) from an inner domain. In this inner domain no resolvable fluid drainage pathways are created and gypsum is essentially stable. The stability of gypsum

Florian Füsseis 1/17/12 12:36 PM

Deleted: '

Florian Füsseis 1/17/12 12:36 PM

Deleted: '

ahead of the dehydration front can be explained with the well-known pressure-dependence of the reaction. Karrech et al. (in prep.) recently revised experimental data by McConnell et al. (1987) and showed that, at 388 K, gypsum is stable at pressures of > 53 MPa. Karrech et al. (in prep.) demonstrate that the primary pressure source for reaction suppression in the sample interior derives from internal stresses due to the anisotropic thermal expansion of gypsum (cf. Ballirano and Melis, 2009).

We interpret the slightly increasing background porosity in the sample interior (Figure 4) to indicate that the reaction commences in the inner domain wherever water can drain into pre-existing pores or thermal cracks (Olgaard et al. 1995, Ko et al. 1997). As previously recognized, the resulting local increase in pore fluid pressure will help to suppress the reaction. However, our data also indicate that any pores that form ahead of the dehydration front remain largely below the resolution limit of about 1 μm , and that they do not destabilize the slow advancement of the dehydration front. The reaction is suppressed until the dehydration front has approached.

We interpret that gypsum breakdown and pore formation are very efficient once the dehydration front has approached to within about 100 μm , or roughly one average grain diameter. We postulate that the key processes during dehydration are intrinsically coupled in a feedback loop related to pressure changes across the dehydration front. At the dehydration front, the thermal-elastic internal and fluid-induced stresses are no longer in static equilibrium, and pore fluid that was previously trapped in pores is released into the drainage system. The resulting pressure drop drives the reaction, i.e. the dehydration of gypsum, which produces new pore space and consequently advances the dehydration front. This feedback operates on a grain-by-grain basis and controls the advancement rate of the dehydration front.

Our model for the dehydration of polycrystalline gypsum conflicts with an important aspect of the model by Olgaard et al., (1995) and Ko et al. (1997). Based on post-experimental observations from thin sections they interpret that the reaction products and their porous haloes grow to diameters of tens of μm throughout the sample before they interconnect and the fluid drains. In our three-dimensional data set we do not observe isolated nuclei of that size ahead of the dehydration front, and we therefore believe that Ko et al. possibly interpreted an oblique section through a very irregular but narrow reaction front.

Florian Fusseis 1/17/12 12:36 PM

Deleted: Our analysis confirms

Florian Fusseis 1/17/12 12:36 PM

Deleted: We believe that the slightly increasing background porosity in the sample interior (Figure 4) is the expression of such dehydration nuclei.

Florian Fusseis 1/17/12 12:36 PM

Deleted: micron

Florian Fusseis 1/17/12 12:36 PM

Deleted: run-away interconnection of such pore space does

Florian Fusseis 1/17/12 12:36 PM

Deleted: occur

Florian Fusseis 1/17/12 12:36 PM

Deleted: , which marks a critical length scale for the reaction.

Florian Fusseis 1/17/12 12:36 PM

Moved (insertion) [1]

Florian Fusseis 1/17/12 12:36 PM

Deleted: As

Florian Fusseis 1/17/12 12:36 PM

Deleted: is controlled on the grain scale, this model does not explain

Florian Fusseis 1/17/12 12:36 PM

Deleted: expulsion behaviour observed by Ko et al.

Florian Fusseis 1/17/12 12:36 PM

Moved up [1]: (1997).

Florian Fusseis 1/17/12 12:36 PM

Deleted: However, it seems also applicable to explain observations made during the dehydration of serpentinite (Llana-Fúnez et al., 2007).

Florian Fusseis 1/17/12 12:36 PM

Deleted: model, the feedback operates on a grain-by-grain basis and no run-away effects occur. In our experiment, fluid expulsion rate is proportional to the rate at which the unreacted domain shrinks. Figure 4 shows that 50% of the sample area in horizontal cross-

Florian Fusseis 1/17/12 12:36 PM

Deleted: reacts within the first 17 minutes. Hence, the highest fluid expulsion rates are expected at the onset of the experiment. The

706
 707 An obvious difference between our and previous studies done with Volterra
 708 alabaster is the lacking confinement of our sample, which leaves it free to drain
 709 through most of its surface. Other investigators generally applied at least some
 710 confining pressure, limited drainage to one end of the cylinder and controlled the
 711 pore fluid pressure (Olgaard et al., 1995, Stretton, 1996, Ko et al., 1997, Miller et
 712 al., 2003, Llana-Fúnez et al., submitted). The drainage configuration certainly
 713 affects the overall geometry of the dehydration front in the sample, and both
 714 pressure sources control compaction in the outer domain and contribute to
 715 thermal-elastic internal stresses. However, our observations of a very narrow
 716 dehydration front with a steep porosity increase are strikingly similar to those
 717 made by Stretton (1996), who conducted her experiments under very similar
 718 conditions than Olgaard et al. (1995) and Ko et al., (1997). We interpret this to
 719 indicate that neither the drainage configuration nor a moderate confining
 720 pressure fundamentally change the breakdown behaviour of polycrystalline
 721 gypsum.

722
 723 The dimensions of the dehydration front and the porosity evolution as observed
 724 in our data are in conflict with those modelled by Wang and Wong (2003). These
 725 authors postulate a smooth porosity increase of about 8% over a sample length
 726 of 25 mm (cf. their figure 7b). The reasons for this disparity remain to be
 727 clarified. In a companion paper (Karrech et al., in prep.), we develop a theory that
 728 captures the advance of the dehydration front on the basis of the dissipative
 729 mechanisms underlying the above feedback, and successfully reproduce both the
 730 sharp dehydration front and its progress over time.

731
 732 In brief, this theory describes the advance of the reaction front as a pressure
 733 diffusion process, accounting for thermal-elastic internal and fluid-induced
 734 stresses in a coupled manner. The linear diffusion constant governing the
 735 advance of the dehydration front due to pressure diffusion can be derived from
 736 our experiment by fitting the front propagation data with Eq. 1 (Figure 5b). We
 737 obtain a value of $8,290 \times 10^{-11} \text{ m}^2\text{s}^{-1}$ ($r^2 = 0.71$). The spread of the data in Figure
 738 5b is due to the undulations of the dehydration front and its asymmetric
 739 progress (Figures 2 and 5a). As discussed in the following section, both front
 740 undulations and asymmetric propagation are most likely a result of the
 741 lattice/fabric control of gypsum breakdown and porosity formation. The
 742 resulting data spread implies that our sample cannot be regarded as a
 743 homogeneous medium on the length scale of the sample radius. However, we
 744 calculated the percentage of reacted sample area in horizontal cross section over

Florian Fusseis 1/17/12 12:36 PM
Deleted: , is the largest difference between our and previous studies.

Florian Fusseis 1/17/12 12:36 PM
Deleted: externally

Florian Fusseis 1/17/12 12:36 PM
Deleted: Both

Florian Fusseis 1/17/12 12:36 PM
Deleted: This additional mechanical loading might explain the difference

Florian Fusseis 1/17/12 12:36 PM
Deleted: fluid expulsion behaviour. ... [2]

Florian Fusseis 1/17/12 12:36 PM
Deleted:), who proposed an empirical relationship between the dehydration rate and porosity generation. While their model captures many of the measurements of Ko et al. (1997), we do see discrepancies in the scales of the dehydration front and porosity evolution. Wang and Wong (2003)

Florian Fusseis 1/17/12 12:36 PM
Deleted: However, similarly to Stretton (1996), our data clearly show a very narrow dehydration front with a steep porosity increase of up to 30% over a distance of less than 150 μm (Figures 2, 4). Whether

Florian Fusseis 1/17/12 12:36 PM
Deleted: is caused by our choice of a millimetre-sized sample or an oversimplification in the underlying empirical model of Wang and Wong (2003) remains

time assuming a perfectly concentric reaction progress and using the diffusion constant obtained here and compared it to the percentage of reacted sample area determined in the physical experiment. Theoretical prediction and measured data match very well (Suppl. Figure 4). This might indicate that our small sample approaches statistical homogeneity with regards to microstructure at the scale of the entire sample cylinder. However, determining the representative elementary volume for Volterra alabaster is beyond the scope of this work. The diffusion constant determined here should therefore be understood as rough estimate with an uncertainty of plus/minus one order of magnitude (see also Figure Rose of Diffusivities). Nevertheless, it constitutes a material property than can be employed to predict the progress of the dehydration front in drained, unconfined gypsum.

4.2 Gypsum breakdown and porosity formation

We interpret the highly anisotropic gypsum lattice to control the actual breakdown process as well as the shapes of the pore nuclei in a similar way as it controls the formation of hemi-hydrate. Sipple et al. (2001) show that hemi-hydrate forms a pseudomorph after the parent gypsum crystal. Hildyard et al. (2011) observed the inheritance of a crystal preferred orientation in hemi-hydrate from parental gypsum and they employ Freyer and Voigt (2003), who predict a topotactic growth relationship between the two minerals. Finally, Finot et al. (1997) documented dehydration of gypsum in-situ and observed a remarkable mobility of water molecules along the (010) lattice planes, outlining preferred evacuation pathways that must have been provided by intracrystalline pores. Combining these observations, and considering the volume change that is involved in the formation of hemi-hydrate, it seems likely that pores that nucleate on the lattice scale follow the crystallographic orientation of their parental grains. We interpret our observation that the observed front irregularities (Figure 2) and the characteristic width of the dehydration front (Figure 4) are of similar size as the mean grain size (Table 1) as indirect evidence for the crystallographic control of dehydration at the grain scale.

We expect the orientation of gypsum grains to control the advance and organization of the dehydration front in a polymineralic gypsum rock (Figure 14). In volumes that exhibit a high degree of fabric anisotropy, which Volterra alabaster does on the millimetre scale according to our analysis (Suppl. Figure 1, Table 1), the dehydration should advance faster in the direction of the (010) lattice planes (Finot et al., 1997). We interpret our data to reflect such a pre-existing anisotropic fabric in parts of the sample: (1) the orientation of pre-

Florian Füsseis 1/17/12 12:36 PM

Deleted: part

existing pores in the sample is highly anisotropic (Figure 11a), and new pores follow this orientation (Figure 11b, c); and (2) the progress of the dehydration front is highly asymmetric (Figure 5a, c). A pre-existing fabric would also align grain boundaries and thermal-elastic damage. We interpret the observed plumes to map such zones of enhanced drainage. An alternative possibility to explain the anisotropy would be heat loss through the thermocouple and the cement that was used to hold it in place. However, due to the small sample dimension and the very effective heater we consider this unlikely.

Once the dehydration front has passed, the porosity consolidates rapidly and does not change significantly anymore. The cumulative pore size frequency distribution over time (Figure 8) shows that, upon the initiation of dehydration, pores rapidly merge into a single cluster of interconnected pores (Figure 9, Suppl. Figure 4). This cluster connects the advancing reaction front with the outer surface of the unconfined sample.

Hildyard et al. (2011) describe networks of reacted and partly reacted material. They interpret the networks to delineate 'large-scale fluid pathways' during the advance of a dehydration front. The porous plumes we observed in our data are potentially related to these structures. A notable difference is that the plumes in our experiment encompass much smaller volumes compared to the networks in Hildyard et al.'s experiment (several hundreds of μm , cf. their Figure 3b). However, we found no evidence that drainage in our sample is controlled by some sort of hierarchical porous network but rather by the interconnected pore cluster shown in Figure 9 and Suppl. Figure 4.

4.3 Data processing

The automated segmentation of grey scale images to isolate pores from their matrix is a critical processing step in the quantitative analyses of microtomographic data. Histogram-based thresholding is a rather simple method (Kaestner et al., 2008) and algorithms that utilize higher order information are generally favoured (e.g. Porter and Wildenschild, 2010, Wang et al., 2011). However, the intrinsic complexity of tomographic data generated from metamorphic rocks (which is constituted by the very large number of objects, their complicated shapes and wide range of size distributions, as well as the complex relationship to other phases) often renders advanced, feature-based techniques too difficult to use and computationally very expensive. Binary thresholding is a computationally efficient alternative.

Florian Füsseis 1/17/12 12:36 PM

Deleted: microns

850 All our SRμCT data suffer from an intrinsic discretization error, which arises
 851 from the use of cubic voxels to represent real objects (e.g. Arns et al., 2002). This
 852 error affects all volumetric analyses we conducted. We designed our
 853 shrinking/expansion experiment to assess the largest possible error resulting
 854 from discretization and emphasize that the error estimates provided are
 855 certainly exaggerated. We stress that the excellent coincidence of the determined
 856 porosities (24-25 %, Table 2) with the theoretically expected porosity (29 %,
 857 assuming no compaction) indicate that our approach and the thresholds we
 858 chose deliver very good first-order results.

860 5. Conclusions

861 The dehydration of polycrystalline gypsum is often considered a proxy for
 862 metamorphic devolatilisation. Current models for dehydration under drained
 863 conditions are based on indirect measurements and post-experimental
 864 assessment of experimental charges in 2D. We conducted an in-situ Synchrotron
 865 X-ray microtomography experiment to document the dehydration of a 2.3 mm
 866 diameter cylinder of polycrystalline gypsum to overcome these limitations. We
 867 use a novel routine to segment porosity from the tomographic time-series data.
 868 The routine is based on time-dependent changes to the grey value distribution
 869 amongst cubic voxels of 2.197 μm³ that record the absorption of x-rays in the
 870 sample. Our workflow allows determining position, shape, volume and
 871 orientation of each individual pore and quantifying percolation over multiple
 872 scales.
 873 We show that the dehydration initiates across a sharp dehydration front. The
 874 front slowly propagates inward from the margin of the unconfined cylinder over
 875 more than four hours. The slow advance of the front is strongly non-linear and
 876 can be fitted with a linear diffusion equation yielding a diffusivity of 8,290 x 10⁻¹¹
 877 m²s⁻¹. The dehydration front delimits an unreacted inner domain, where no
 878 resolvable porosity could be observed, from an outer domain where anisotropic
 879 pores form. The non-random orientation of these pores can be explained by a
 880 preexisting fabric in the sample. Behind the dehydration front, isolated pores
 881 rapidly link to a large interconnected cluster of pores that connects to the
 882 outside of the sample at all times, providing a tortuous drainage pathway.
 883 We interpret gypsum in the inner domain to be stabilized by increased
 884 pressures. These likely result from the thermal expansion of gypsum and locally
 885 increased pore fluid pressures. Across the dehydration front, gypsum breakdown
 886 is very efficient and most likely controlled by the orientation of the gypsum
 887 lattice with respect to the advancing front. Gypsum breakdown initiates steadily
 888 grain by grain. We combine our observations in a model, in which the

Florian Füsseis 1/17/12 12:36 PM

Deleted: Our

Florian Füsseis 1/17/12 12:36 PM

Deleted: documents

Florian Füsseis 1/17/12 12:36 PM

Deleted: . Using

Florian Füsseis 1/17/12 12:36 PM

Deleted: , we

Florian Füsseis 1/17/12 12:36 PM

Deleted: the basis of

Florian Füsseis 1/17/12 12:36 PM

Deleted: records

Florian Füsseis 1/17/12 12:36 PM

Deleted: at the margin of the unconfined cylinder. A

Florian Füsseis 1/17/12 12:36 PM

Deleted: radially

Florian Füsseis 1/17/12 12:36 PM

Deleted: forms. No run-away behavior is

Florian Füsseis 1/17/12 12:36 PM

Deleted: . In

Florian Füsseis 1/17/12 12:36 PM

Deleted: , gypsum seems

Florian Füsseis 1/17/12 12:36 PM

Deleted: , which

Florian Füsseis 1/17/12 12:36 PM

Deleted: We interpret the breakdown to occur where the pressure is relieved. Anisotropic pores form, whose non-random orientation can be explained by a preexisting fabric in the sample. Pores rapidly link to a large interconnected cluster of pores, that connects to the outside of the sample at all times, providing an efficient drainage pathway.

dehydration of polycrystalline gypsum is controlled by a feedback of pressure release and pore formation on the grain scale. In a companion paper (Karrech et al., in prep.), we develop a theory that describes the advance of the dehydration front based on the dissipative mechanisms involved.

Acknowledgments

This work was supported by the Western Australian State Government through the Premier's Fellowship Program and the Western Australian Geothermal Centre of Excellence Program, and the Australian Synchrotron Research Program, funded by the Commonwealth of Australia under the Major National Research Facilities Program. Use of the Advanced Photon Source at Argonne National Laboratory was supported by the U. S. Department of Energy, Office of Science, Office of Basic Energy Sciences, under Contract No. DE-AC02-06CH11357. SLF acknowledges funding by NERC, grant NE/C002938/1, and by Spanish Ministerio de Ciencia e Innovación, grant RYC-2008-02067. CS acknowledges funding by the German Research Foundation under Grant No. SCHR 1262/1-1. We thank iVEC@UWA in Perth for use of their computing facilities. We thank S. Revets for making unpublished results available and K. Gessner, and R. Hough for help with data acquisition. Reviews by H. Milsch and F. Trippetta helped to improve the manuscript and are gratefully acknowledged.

6. References

- Arns, C. H., Knackstedt, M.A. Val Pinczewski, W., Garnoczi, E.J.: Computation of linear elastic properties from microtomographic images: Methodology and agreement between theory and experiment, *Geophysics*, 67/5, 1396-1405, 2002.
- Ballirano, P. and Melis, E.: Thermal behaviour and kinetics of dehydration of gypsum in air from in situ real-time laboratory parallel-beam X-ray powder diffraction, *Phys. Chem. Min.* 36, 391-402, 2009.
- Banhart, J.: *Advanced Tomographic Methods in Materials Research and Engineering*, Oxford University Press, USA, 2008.
- Bezou, C., Nonat, A., Mutin, J.-C., Christensen, A.N., Lehmann, M.S.: Investigation of the crystal structure of γ -CaSO₄, CaSO₄·0.5 H₂O, and CaSO₄·0.6 H₂O by powder diffraction methods, *J. Solid State Chem.* 117, 165-176, 1995.
- Charola, A.E., Pühringer, J., Steiger, M.: Gypsum: a review of its role in the deterioration of building materials, *Environ Geol*, 52, 339-352, 2007.
- Christensen, A.N., Olesen, M., Cerenius, Y., Jensen, T.R.: Formation and Transformation of Five Different Phases in the CaSO₄-H₂O System: Crystal Structure of the Subhydrate β -CaSO₄ · 0.5H₂O and Soluble Anhydrite CaSO₄,

Florian Füsseis 1/17/12 12:36 PM

Deleted: The slow, strongly non-linear advance of the dehydration front can be fitted with a linear diffusion equation yielding a diffusivity of $8,290 \times 10^{-11} \text{ m}^2\text{s}^{-1}$.

Florian Füsseis 1/17/12 12:36 PM

Formatted: Font:Bold

Florian Füsseis 1/17/12 12:36 PM

Formatted: English (UK)

Florian Füsseis 1/17/12 12:36 PM

Formatted: English (UK)

954 Chem. Mater. 20, 2124-2132, 2008.

955 Clauser, C. and Huenges, E.: Thermal conductivity of rocks and minerals, in: Rock
 956 Physics and Phase Relations, A Handbook of Physical Constants, AGU
 957 Reference Shelf 3, AGU, Washington, USA, 105 - 126, 1995.

958 Finot, E., Lesniewska, E., Mutin, J.-C., Goudonnet, J.-P.: Reactivity of gypsum faces
 959 according to the relative humidity by scanning force microscopy, Surface
 960 Science, 384, 201-217, 1997.

961 Freyer, D. and Voigt, W.: Crystallization and Phase Stability of CaSO_4 and CaSO_4 -
 962 Based Salts, Monatsh. Chem. 134, 693-719, 2003.

963 Freyer, D. and Voigt, W.: Can mixtures of α - and β -hemihydrates be quantified by
 964 means of thermoanalysis? ZKG Int. 62, 3, 47-53, 2009.

965 Hacker, B.R.: Diagenesis and fault valve seismicity of crustal faults, JGR 102, B11,
 966 24459-24467, 1997.

967 Heard, H.C. and Rubey, W.W.: Tectonic implications of gypsum dehydration, Geol.
 968 Soc. Am.Bull., 77, 741-760, 1966.

969 Hildyard, R.C., Llana-Fúnez, S., Wheeler, J., Faulkner, D.R., Prior, D.J.: Electron
 970 Backscatter Diffraction (EBSD) Analysis of Bassanite Transformation Textures
 971 and Crystal Structure Produced from Experimentally Deformed and
 972 Dehydrated Gypsum, J. Petrol., 52, 5, 839-856, 2011.

973 Jacques, S.D.M., González-Saborido, A., Leynaud, O., Bensted, J., Tyrer, M., Greaves,
 974 R.I.P., Barnes, P.: Structural evolution during the dehydration of gypsum
 975 materials, Min. Magaz. 73, 3, 421-432, 2009.

976 Kaestner, A., Lehmann, E., Stampanoni, M.: Imaging and image processing in
 977 porous media research, Adv. Water Resour., 31, 1174-1187, 2008.

978 Karrech, A., Regenauer-Lieb, K., Schrank, C., Füsseis, F.: Dehydration of
 979 polycrystalline gypsum, a theoretical and numerical investigation based on
 980 first order thermodynamic principles, in prep.

981 Ko, S., Olgaard, D.L., Wong, T.-F., Generation and maintenance of pore pressure
 982 excess in a dehydrating system 1. Experimental and microstructural
 983 observations, JGR, 102, B1, 825-839, 1997.

984 Launeau, P., Archanjo, C.J., Picard, D., Arbaret, L., Robin, P.-Y.: Two- and thre-
 985 dimensional shape fabric analysis by the intercept method in grey levels,
 986 Tectonophysics, 492, 230-239, 2010.

987 Liu, J., Regenauer-Lieb, K., Hines, C., Liu, K., Gaede, O., Squelch, A.: Improved
 988 estimates of percolation and anisotropic permeability from 3-D X-ray
 989 microtomography using stochastic analyses and visualization, Geochem.
 990 Geophys. Geosy., 10, 5, doi: 10.1029/2008GC002358, 2009.

991 Liu, J., Regenauer-Lieb, K.: Application of percolation theory to
 992 microtomography of structured media: Percolation threshold, critical

993 exponents, and upscaling, Phys. Rev. E, 83, 016106, 2011.
 994 Llana-Fúnez, S., Brodie, K.H., Rutter, E.H., Arkwright, J.C.: Experimental
 995 dehydration kinetics of serpentinite using pore volumetry, J. metamorphic
 996 Geol., 25, 423-438, 2007.
 997 Llana-Fúnez, S., Wheeler, J., Faulkner, D.R.: The influence of confining pressure
 998 during metamorphism: dehydration experiments with gypsum, Contrib.
 999 Mineral. Petr., submitted.
 1000 McConnell, J.D.C., Astill, D.M., Hall, P.L.: The pressure dependence of the
 1001 dehydration reaction of gypsum, Mineral. Mag. 51, 453-457, 197.
 1002 Miller, S.A., van der Zee, W., Olgaard, D.L., Connolly, J.A.D.: A fluid-pressure
 1003 feedback model of dehydration reactions: experiments, modeling, and
 1004 application to subduction zones, Tectonophysics 370, 241-251, 2003.
 1005 [Milsch, H.H. and Scholz, C.H.: Dehydration-induced weakening and fault slip in](#)
 1006 [gypsum: Implications for the faulting process at intermediate depth in](#)
 1007 [subduction zones, J. Geoph. Res 110, B04202, doi:10.1029/2004JB003324,](#)
 1008 [2005.](#)
 1009 Murrell, S.A.F. and Ismail, I.A.H.: The effect of decomposition of hydrous minerals
 1010 on the mechanical properties of rocks at high pressures and temperatures,
 1011 Tectonophysics 31, 207-258, 1976.
 1012 Olgaard, D.L., Ko, S., Wong, T.-F.: Deformation and pore pressure in dehydrating
 1013 gypsum under transiently drained conditions, Tectonophysics 245, 237-248,
 1014 1995.
 1015 Regenauer-Lieb, K. and Yuen, D.: Positive feedback of interacting ductile faults
 1016 from coupling of equation of state, rheology and thermal-mechanics, PEPI,
 1017 142, 113-135, 2004.
 1018 [Schmidt, H., Paschke, I., Freyer, D., Voigt, W.: Water Channel Structure of](#)
 1019 [Bassanite at High Air Humidity: Crystal Structure of \$\text{CaSO}_4 \cdot 0.625\text{H}_2\text{O}\$, Acta](#)
 1020 [Crystl B67, 467-475, with corrigendum in B68, 2011.](#)
 1021 Singh, N.B. and Middendorf, B.: Calcium sulphate hemihydrate hydration leading
 1022 to gypsum crystallization, Prog. Cryst. Growth Ch., 53, 57-77, 2007.
 1023 Stauffer, D. and Aharony, A.: Introduction to Percolation Theory (2nd edition),
 1024 Taylor & Francis Ltd., London, 1994.
 1025 Sprunt, E.S. and Brace, W.F.: Direct Observation of Microcavities in Crystalline
 1026 Rocks, Int. J. Rock Mech. Min. Sci. & Geomech. Abstr. 11, 139 -150, 1974.
 1027 Stock, S.R.: Microcomputed Tomography, Methodology and Applications, Taylor
 1028 & Francis Ltd, London, 2009.
 1029 Stretton, I.C.: An experimental investigation of the deformation properties of
 1030 gypsum, PhD thesis, Univ. Manchester, 1996.
 1031 Wang, W.-H. and Wong, T.-F.: Effects of reaction kinetics and fluid drainage on

1032 the development of pore pressure excess in a dehydrating system,
1033 Tectonophysics 370, 227-239, 2003.
1034 Wang, W., Kravchenko, A.N., Smucker, A.J.M., Rivers, M.L.: Comparison of image
1035 segmentation methods in simulated 2D and 3D microtomographic images of
1036 soil aggregates, Geoderma, 162, 231-241, 2011.

1037

1038 **Tables**

1039 **Table 1** – Grain size and anisotropy characterization of the sample material.

1040

1041 | **Table 2** – Porosities, total number of pores, the volume of the largest and second
1042 largest pore in the parallelepiped at different times during the experiment. See
1043 text for discussion.

1044

1045

Florian Füsseis 1/17/12 12:36 PM

Deleted: .

Figure captions

Figure 1 – To-scale sketch of the experimental set-up used within the X-ray beam configuration.

Figure 2 – Vertical cross section through the sample at different times during the experiment (depicted in the four quadrants). The grey values correspond to the absorption of x-rays, pores appear dark grey to black. The white stippled frame outlines the location of the parallelepiped in which porosity was quantified (see text and also Suppl. Figure 5).

Figure 3 – Histograms of the grey value distributions amongst the 180×10^6 voxel constituting the parallelepiped in which porosity was quantified, at different times during the experiment. The vertical stippled line indicates the critical threshold we used for segmenting porosity.

Figure 4 – Distribution of porosity along a radius at 10, 70 and 130 minutes. Note the slightly increasing background porosity in the inner domain. Values exceeding 30 % porosity result from the comparatively small sampling volume used to determine the porosity values shown.

Figure 5 – The advance of the dehydration front, a) the position of the dehydration front in a horizontal section through the sample at different times during the experiment; b) the slow, highly non-linear radial progress of the front over time quantified from horizontal and vertical sections through the sample. See text for explanation of the technique. c) rose plot of linear diffusion constants derived from fitting Eq. 1 to propagation of dehydration front along radii in two horizontal cross sections through the sample. The higher diffusion coefficients probably relate to a pre-existing alignment of gypsum in part of the sample, as discussed in the text. Measurement strategy is explained in text (compare Suppl. Figure 3).

Figure 6 – Porosity quantification in the parallelepiped outlined in Figure 2 and Suppl. Figure 5; a) Total porosity over time. Grey squares are the porosity values we determined using the threshold value derived from changes in the grey value histograms (Figure 3). The values correspond agreeably well with the theoretically predicted 30%. White and black squares, respectively, are the largest possible errors based on the numerical expansion/shrinking experiment which is explained in the text. b) Total number of pores over time. Note that the value consolidates as soon as the dehydration front has propagated through the

Florian Füsseis 1/17/12 12:36 PM

Deleted: x

Florian Füsseis 1/17/12 4:45 PM

Formatted: Font:12 pt

Florian Füsseis 1/17/12 4:45 PM

Formatted: Font:12 pt

Florian Füsseis 1/17/12 4:45 PM

Deleted: Porosity evolution along a radius that crosscuts the dehydration front perpendicularly, at three different times during the experiment. Note the slightly increasing background porosity in the inner domain. Values exceeding 30 % porosity result from the comparatively small and non-representative sampling volume used to quantify porosity.

Florian Füsseis 1/17/12 12:36 PM

Deleted: position

Florian Füsseis 1/17/12 12:36 PM

Deleted: in different directions

Florian Füsseis 1/17/12 12:36 PM

Deleted: set of

Florian Füsseis 1/17/12 12:36 PM

Deleted: porosity values that resulted from

Florian Füsseis 1/17/12 12:36 PM

Deleted: .

1102 | sampling volume (after 130 min). White and black squares, respectively, are the
 1103 | largest possible errors derived from the numerical expansion/shrinking
 1104 | experiment. See text for further explanation.

1106 | **Figure 7** – Absolute pore size frequency distribution over time. The distribution
 1107 | consolidates as soon as the dehydration front has passed through the sampling
 1108 | volume (after 130 min).

1110 | **Figure 8** – Cumulative porosity size frequency distribution over time. The
 1111 | distribution is dominated by a single cluster of interconnected pores that makes
 1112 | up more than 90 per cent of the total porosity.

1114 | **Figure 9** – Horizontal section through the sample cylinder illustrating the largest
 1115 | interconnected pore cluster (in yellow) at different times during the experiment.
 1116 | Each quadrant shows the extent of the cluster at the time given by the number,
 1117 | the stippled line indicates the extent of the cluster 60 minutes earlier (in red).
 1118 | The sample diameter is 2.3 mm. The white frame indicates the location of the
 1119 | parallelepiped in which porosity was quantified.

1121 | **Figure 10** – Isotropy index over size of all pores [50; 450 voxel], [110; 989 μm^3]
 1122 | after 130 (left) and 310 minutes (right). Color-coded contours indicate data
 1123 | point density in per cent (calculated for moving search windows of size 50 voxel
 1124 | x 0.01 isotropy index units for a step size of 1 voxel in horizontal direction and
 1125 | 0.005 isotropy index units in vertical direction). Note that all pores are clearly
 1126 | anisotropic ($I_i < 1$) in shape with most pores having indices between 0.2 and 0.4.
 1127 | This trend does not change with time.

1129 | **Figure 11** – Stereo plots showing the orientations of the longest principal axis of
 1130 | pores of different sizes. a) Orientations prior to heating, contours calculated from
 1131 | pores between 51 and 300 voxel, circles denote pores between 51 and 300 voxel
 1132 | in volume; b) Orientations after 70 minutes, contours are calculated from pores
 1133 | between 51 and 150 voxel, black circles are orientations of pores between 151
 1134 | and 300 voxel and green circles of pores between 301-450 voxel; and c)
 1135 | Orientations after 310 minutes, contours are calculated from pores between 51
 1136 | and 150 voxel, black circles are orientations of pores between 151 and 300 voxel
 1137 | and orange circles of pores between 301-450 voxel. The plots indicate that a pre-
 1138 | existing anisotropy controls the orientation of pores before and during
 1139 | dehydration.

Florian Füsseis 1/17/12 12:36 PM

Deleted: total numbers of pores we

Florian Füsseis 1/17/12 12:36 PM

Deleted: Porosity

Florian Füsseis 1/17/12 12:36 PM

Deleted: See text for explanation.

Florian Füsseis 1/17/12 12:36 PM

Deleted: See text for explanation

Florian Füsseis 1/17/12 12:36 PM

Moved (insertion) [2]

Florian Füsseis 1/17/12 12:36 PM

Deleted: Figure 9

Florian Füsseis 1/17/12 12:36 PM

Moved down [3]: – Three-dimensional visualization of the morphology of the largest interconnected pore cluster at the reaction front – requires red-cyan glasses. Note the complexity of the pore shape. Side length of the cube shown is 200 voxel (260 μm).

Florian Füsseis 1/17/12 12:36 PM

Formatted: Font: Cambria

Florian Füsseis 1/17/12 12:36 PM

Deleted: ... [3]

Florian Füsseis 1/17/12 12:36 PM

Deleted: 1200

Florian Füsseis 1/17/12 12:36 PM

Deleted: 2640

Florian Füsseis 1/17/12 12:36 PM

Deleted: percent

Florian Füsseis 1/17/12 12:36 PM

Deleted: 25

Florian Füsseis 1/17/12 12:36 PM

Deleted: 310-140

Florian Füsseis 1/17/12 12:36 PM

Deleted: 310-140 voxel. See text for interpretation

1162 **Figure 12** – Porosity frequency distribution amongst cubes with a 50-voxel side
 1163 length sampled throughout the parallelepiped at different times during the
 1164 experiment (see text for explanation). The shapes of the peaks give an indication
 1165 of how homogeneously porosity is distributed within the sample, with the
 1166 vertical lines marking the total porosity measured at different times. After 130
 1167 minutes the porosity distribution within the parallelepiped is relatively
 1168 homogeneous.

1169

1170 **Figure 13** – Probability functions for percolation in the three principal
 1171 directions amongst cubes with a 50-voxel side length placed in the
 1172 parallelepiped. Each of the four diagrams compares two consecutive time steps.
 1173 Dotted lines – x-axis, stippled line, y-axis, solid line – z-axis. Note that from 130
 1174 minutes onward, all cubes with more than about 22 % porosity are percolating
 1175 in all three directions. In all cubes with a smaller porosity, the x-direction is most
 1176 likely to percolate.

1177

1178 **Figure 14** – Sketch map illustrating the grain-by-grain advance of the
 1179 dehydration front and the effect of the strong crystallographic anisotropy of
 1180 gypsum. See text for discussion.

1181

1182 **Suppl. Figure 1** – Left: Photographs of thin sections of Volterra alabaster in
 1183 polarized light with crossed polarizers. Right: Shape-fabric ellipsoids calculated
 1184 with the line-intercept code by Launeau et al. (2010). Step size of rotation angle
 1185 is 10°; normal distance between search grid lines is 5 pixel. The largest mean
 1186 grain size in the orientation interval [0°; 360°] is denoted by a (long axis of the
 1187 fabric ellipsoid) while the smallest mean grain size is b (short axis of the fabric
 1188 ellipsoid). R is the aspect ratio of the ellipsoid. The fabric ellipsoids show that
 1189 Volterra gypsum exhibits a shape-preferred orientation locally.

1190

1191 **Suppl. Figure 2** – Temperature-Time curve of the experiment. Note that the
 1192 tomographic data were acquired at 325 K after each heating period.

1193

1194 **Suppl. Figure 3** - Measurement strategy for the progress of the dehydration
 1195 front over time from horizontal (upper panel) and vertical (lower panel)
 1196 tomography slices. The global coordinate system is indicated on the right-hand
 1197 side of the figure. Measurements of front position over time (as described in the
 1198 text) are performed with a simple image analysis routine on binary images. The
 1199 binary images are produced from the tomography data to segment unreacted
 1200 from reacted material. The outer margin of the sample is easily separated from

Florian Füsseis 1/17/12 12:36 PM

Deleted: placed in

Florian Füsseis 1/17/12 12:36 PM

Deleted: Vertical

Florian Füsseis 1/17/12 12:36 PM

Deleted: mark

Florian Füsseis 1/17/12 12:36 PM

Deleted: explanation

Florian Füsseis 1/17/12 12:36 PM

Deleted: from

1206 the background (not shown; compare Fig. 2) by binary thresholding (accuracy is
1207 +/- 1 pixel). The position of the front at a given time, however, is determined by
1208 manual digitization. We estimate that the accuracy of this procedure is +/- 3
1209 pixel (i.e., < 5 μm).

1211 **Suppl. Figure 4** - Plot of proportions of sample area where reaction has initiated
1212 for two horizontal tomography slices (A and B) as a function of time. Note that in
1213 slice A the reaction initiation front has reached the centre of the cylinder before
1214 the last scan. Black solid line denotes calculation of reaction initiation progress
1215 assuming a perfectly concentric front propagation and the diffusivity determined
1216 with equation 1 (compare Fig. 5).

1218 **Suppl. Figure 5** - Three-dimensional visualization of the morphology of the
1219 largest interconnected pore cluster at the reaction front – requires red-cyan
1220 glasses. Note the complexity of the pore shape. Side length of the cube shown is
1221 200 voxel (260 μm).

Florian Füsseis 1/17/12 12:36 PM

Deleted: micron

Florian Füsseis 1/17/12 12:36 PM

Deleted: proportion

Florian Füsseis 1/17/12 12:36 PM

Deleted: reacted

Florian Füsseis 1/17/12 12:36 PM

Deleted: has come to completion

Florian Füsseis 1/17/12 12:36 PM

Moved (insertion) [3]

Florian Füsseis 1/17/12 12:36 PM

Formatted: Font: Cambria

Florian Füsseis 1/17/12 12:36 PM

Moved up [2]: The sample diameter is 2.3 mm. The white frame indicates the location of the parallelepiped in which porosity was quantified.

Florian Füsseis 1/17/12 12:36 PM

Deleted: **Figure 5** – Horizontal section through the sample cylinder illustrating the largest interconnected pore cluster (in yellow) at different times during the experiment. Each quadrant shows the extent of the cluster at the time given by the number, the stippled line indicates the extent of the cluster 60' earlier (in red).